Research Paper

Amorphous NiO as co-catalyst for enhanced visible-light-driven hydrogen generation over g-C$_3$N$_4$ photocatalyst

CrossMark

Jianni Liu[a,b], Qiaohui Jia[a], Jinlin Long[b], Xuxu Wang[b], Ziwei Gao[a,*], Quan Gu[a,b,*]

[a] Key Laboratory of Applied Surface and Colloid Chemistry, Ministry of Education, School of Chemistry and Chemical Engineering, Shaanxi Normal University, Xi'an, 710062, PR China
[b] State Key Laboratory of Photocatalysis on Energy and Environment, Fuzhou University, Fuzhou, 350002, PR China

A B S T R A C T

This study was mainly aimed at constructing an amorphous NiO modified g-C$_3$N$_4$ non-noble metal heterojunction photocatalyst for enhanced visible-light hydrogen evolution. The Ni species modified g-C$_3$N$_4$ sample was firstly prepared through the wetness impregnation method and then the phase and crystallinity of Ni species co-catalysts on g-C$_3$N$_4$ were adjusted by the thermal oxidation at different temperature. The detailed characterizations revealed that the amorphous NiO co-catalysts are supported successfully on g-C$_3$N$_4$, and the C−O−Ni linkages in the amorphous NiO/g-C$_3$N$_4$ heterojunctions are formed at NiO and g-C$_3$N$_4$ interface after annealing at 300 °C. Compared to bare g-C$_3$N$_4$ and crystalline NiO modified g-C$_3$N$_4$ photocatalysts, amorphous NiO modified g-C$_3$N$_4$ non-noble metal photocatalyst showed significantly enhanced visible-light photocatalytic hydrogen production activity. The amorphous NiO co-catalysts provided more active sites for H$_2$ evolution and amorphous NiO modification caused the enhanced visible-light response. Moreover, amorphous NiO/g-C$_3$N$_4$ heterojunctions formed at interface between amorphous NiO and host g-C$_3$N$_4$ created an inner electric field, which allowed for the transfer of the photogenerated electrons of g-C$_3$N$_4$ across the interfacial C−O−Ni linkages to amorphous NiO co-catalysts and thus significantly promoted the migration and separation of photogenerated charge carriers.

1. Introduction

Metal free g-C$_3$N$_4$ polymer material composed of nature abundant elements (C and N) has been regarded as a promising material for photocatalytic H$_2$ evolution because it is non-toxic, low cost, high stability and has excellent optical properties and electronic structure [1–11]. However, the bare g-C$_3$N$_4$ material hardly showed the photocatalytic activity for H$_2$ evolution under visible-light irradiation due to the low separation efficiency and high recombination of photogenerated charge carriers, the high surface overpotential for hydrogen release as well as the lack of surface active sites for H$_2$ evolution. Generally, the noble metal co-catalysts [1,12–16], such as Pt nanoparticles, are loaded on g-C$_3$N$_4$ surface to enhance charge transfer and provide active sites for the H$^+$ reduction and finally to realize photocatalytic hydrogen production over g-C$_3$N$_4$. The introduction of noble metal co-catalysts, however, increases the cost of the photocatalyst, which will greatly limit its practical applications.

Therefore, it is of great importance to develop earth-abundant and low-cost hydrogen evolution co-catalysts as alternatives. Fe, Co, Ni, Cu, Zn, and carbon based materials (iron (III) porphyrin, CoS, Ni(OH)$_2$, NiS, Cu$_2$O, ZnIn$_2$S$_4$, carbon QDs and so on) [8,17–22] have been intensively studied as effective co-catalysts for this purpose. For example, the rate of H$_2$ evolution over g-C$_3$N$_4$ under visible-light illumination was significantly improved after loading with CoS [18]. Yu et al. [19] reported that utilization of low-cost Ni(OH)$_2$ as a substitute for noble metals (such as Pt) in the photocatalytic H$_2$ production for g-C$_3$N$_4$. Liu et al. [21] demonstrated that core@shell Cu$_2$O@g-C$_3$N$_4$ shows efficient visible-light photocatalytic hydrogen evolution and enhanced photostability. However, it was found that the non-noble metal promoters are less effective in improving photocatalytic efficiency compared to noble metal catalysts such as Pt.

It has been also revealed that the photocatalytic activity of co-catalysts modified samples strongly depends on the crystal structure, morphology, especially crystallinity and particle size of co-catalyst. In the research of microstructure of co-catalysts, many of discoveries and breakthroughs have been reported, ranging from crystal to amorphous structure, clusters, even to single atom or single site. For example, Kong et al. [23] developed a novel amorphous CoSn$_x$O$_y$ decorated graphene

nanohybrid photocatalyst, which shows efficient photocatalytic hydrogen evolution. Yuan et al. [24] demonstrated that H_2 evolution activity of CdS is significantly enhanced in the presence of the amorphous Co_3O_4 co-catalyst. Liu et al. [25] grafted Cu(II) oxide amorphous nanoclusters on Ti^{3+} self-doped TiO_2 to improve the visible-light photocatalytic activity. Chen et al. [26] prepared the amorphous NiO modified N/TiO_2 for visible-light photocatalytic hydrogen evolution. They believed that the molecular Ti−O−Ni heterojunctions promote the transfer and separation of photogenerated electrons and holes. Also, Fan et al. [27] reported single-site nickel-grafted anatase TiO_2 for hydrogen production and revealed that the Ti−O−Ni p-n heterojunctions create visible light absorption and photocatalysis. Li et al. [28] found that loading isolated single Pt atoms as co-catalyst on g-C_3N_4 significantly enhances the photocatalytic activity for H_2 evolution. Amorphous structure and clusters (even single atom and single site species), generally, have much smaller bandgap, lack the long-range atomic order and have many defects, which allow for harvesting visible light, promoting charge transfer and providing more active sites for photocatalytic reaction.

Herein, in the present work, we aimed to constructing an amorphous NiO modified g-C_3N_4 non-noble metal heterojunction photocatalyst for enhanced visible-light hydrogen evolution. The Ni species modified g-C_3N_4 sample was annealing at different temperature to control the phase and crystallinity of Ni species co-catalysts on g-C_3N_4. After annealing at 300 °C, the amorphous NiO co-catalysts were formed on g-C_3N_4, and the C−O−Ni linkages in the amorphous NiO/g-C_3N_4 heterojunctions were formed at NiO and g-C_3N_4 interface. For comparison, two kind of crystalline NiO modified g-C_3N_4 samples (Ni/g-C_3N_4-CI and Ni/g-C_3N_4-CH) were prepared by the hydrothermal method and the impregnation method as control samples. Photocatalytic activity results showed that amorphous NiO modified g-C_3N_4 photocatalyst has significantly enhanced visible-light photocatalytic hydrogen production activity as compared to bare g-C_3N_4 and crystalline NiO modified g-C_3N_4 photocatalysts. The results of photocatalytic activity and characterization indicated that the amorphous NiO co-catalysts have great roles in photocatalytic H_2 evolution over g-C_3N_4. First, the amorphous NiO co-catalysts provided more active sites for H_2 evolution. Second, amorphous NiO modification caused the enhanced visible light response. Last, amorphous NiO/g-C_3N_4 heterojunctions allowed for the transfer of the photogenerated electrons of g-C_3N_4 across the interfacial C−O−Ni linkages to amorphous NiO co-catalysts and thus significantly promoted the migration and separation of photogenerated charge carriers.

2. Experimental section

2.1. Preparation of g-C_3N_4

Graphitic carbon nitride (g-C_3N_4) was prepared by thermal polycondensation using melamine and ammonia chloride as precursors according to the reported reference [29]. Typically, 4 g melamine and 10 g ammonia chloride was mixed and ground in a mortar. The mixture was put in a crucible with cover and annealed at 550 °C for 4 h with a heating rate of 4 °C min^{-1} in a muffle furnace.

2.2. Preparation of Ni(OH)$_2$ modified g-C_3N_4

Ni(OH)$_2$ modified g-C_3N_4 was prepared via a facile impregnation method. In a typical process, 1.0 g of g-C_3N_4 powders were dispersed in 50 mL water with continuous stirring in a beaker. Thereafter, a desired amount of nickel chloride solution (20 mg/mL) was added in above suspension under vigorous stirring and then the pH of solution was adjusted to 12.0 using 28.0% ammonia. After stirring overnight, the suspension was dried in the oven.

2.3. Preparation of Ni/g-C_3N_4

Amorphous NiO modified g-C_3N_4 (denoted as Ni/g-C_3N_4) was prepared via post annealing of Ni(OH)$_2$ modified g-C_3N_4. The obtained Ni (OH)$_2$ modified g-C_3N_4 was annealed at different temperature (100 °C, 200 °C, 300 °C, 400 °C, and 500 °C) for 3 h in air and the final products were ground in a mortar to get photocatalysts (denoted as Ni/g-C_3N_4-T, T refers to the annealing temperature: 100, 200, 300, 400, and 500). For the preparation of Ni$_x$/g-C_3N_4 with different NiO contents (x = 0.5, 1.0, 3.0, 5.0, 7.0, 9.0, 10, represents NiO content, NiO wt.% = 0.5%, 1.0%, 3.0%, 5.0%, 7.0%, 9.0%, 10%), added amount of nickel chloride solution (20 mg/mL) is 0.8, 1.6, 4.9, 8.4, 12.0, 15.8, 17.7 mL, respectively.

2.4. Preparation of Ni/g-C_3N_4-C

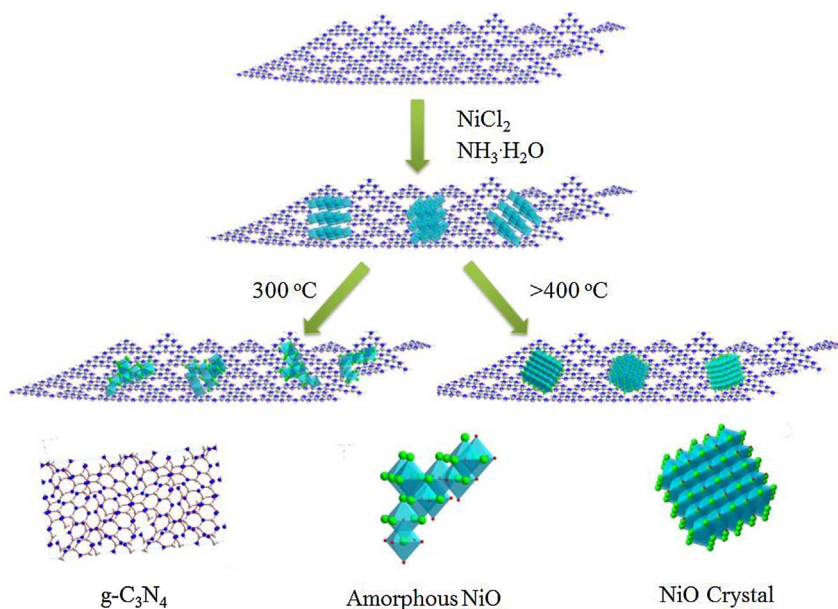For comparison, two kinds of crystalline NiO modified g-C_3N_4 (denoted as Ni/g-C_3N_4-C) was prepared via different treatment process as follows: (1) the sample denoted as Ni/g-C_3N_4-CI was prepared via an impregnation method and post heat treatment. Firstly, a desired amount of nickel chloride solution (20 mg/mL) was added in 50 mL water under vigorous stirring in a beaker and then the pH of solution was adjusted to 12.0 using 28% ammonia. 0.8, 1.6, 4.9, 8.4, 12.0, 15.8, 17.7 mL nickel chloride solution was used for the preparation of Ni$_x$/g-C_3N_4-CI with different NiO contents, where x represent NiO content, NiO wt% = 1.0%, 3.0%, 5.0%, 7.0%, 9.0%, 10%, respectively. Thereafter, 1.0 g of g-C_3N_4 powders were dispersed in above solution with vigorous stirring for 30 min and the powder product was collected via centrifugation, washed with distilled water and ethanol, respectively, and dried at 60 °C in an oven. The final product was obtained after annealing at 300 °C for 3 h in air. (2) the sample denoted as Ni/g-C_3N_4-CH was prepared by a hydrothermal method and post heat treatment. Typically, 1.0 g of g-C_3N_4 powders, 50 mL water, and a desired amount of nickel chloride solution (20 mg/mL) were added in turn into a 100 mL beaker. The pH of solution was adjusted to 10.0 using 28% ammonia with continuous and vigorous stirring for 30 min. Then the solution was put into a 100 mL Teflon-lined autoclave. The autoclave was sealed and maintained at 160 °C for 6 h. After reaction, the powder product was collected via centrifugation, washed with distilled water and ethanol, respectively, and dried at 60 °C in an oven. The final product was obtained after heat treatment at 300 °C for 3 h in air.

2.5. Characterizations

The X-ray Diffraction (XRD) patterns of all samples were collected on Rigaku D/Max2550VB+/PC (Cu Kα source) at a scan rate of 2.4° min^{-1}. Transmission Electron Microscopy (TEM) images and element mapping were obtained by a Tecnai G2 F20 transmission electron microscopy (FEI, USA) at an accelerating voltage of 200 kV. UV–vis Diffuse Reflectance Spectrum (UV–vis DRS) was measured by a UV/vis spectrophotometer (UV-Lambda 950, Perkin Elmer). Fourier Transform Infrared spectra (FTIR) were derived from Perkin Elmer Fourier Transform Infrared Spectrometer GX. Photoluminescence (PL) spectra were accomplished in solid with Shimadzu RF5301 Spectrofuorophotometer with an excitation wavelength of 380 nm. X-ray Photoelectron Spectroscopy (XPS) spectra were determined on a VG ESCALAB 250 XPS system with a monochromatized Al Kα X-ray source (15 kV, 200 W). Nitrogen adsorption-desorption isotherms were performed at 77 K using Micromeritics ASAP 2010 equipment.
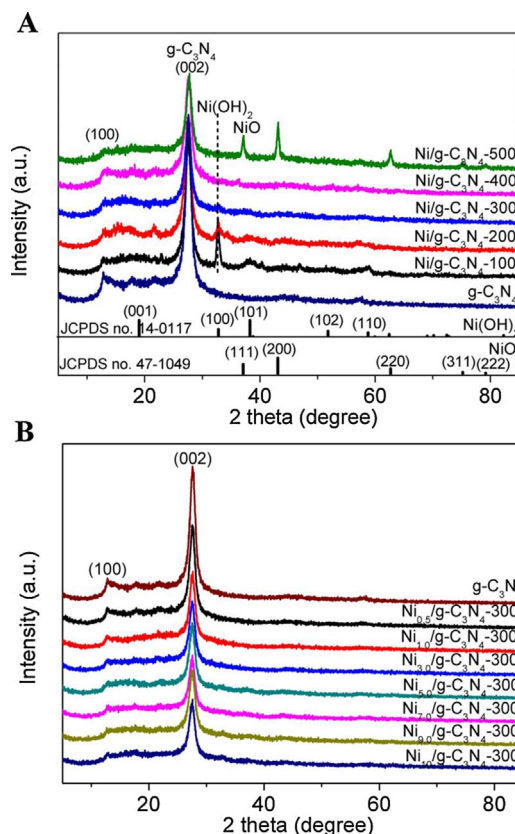
2.6. Photocatalytic H_2 generation

The photocatalytic activities for hydrogen evolution under visible light, UV light, or solar light irradiation were performed in a closed gas-recirculation system equipped with a top-irradiation Pyrex reaction

Fig. 1. The synthetic route of Ni/g-C$_3$N$_4$ composite.

vessel. 0.05 g of the sample was first suspended in 100 mL of aqueous solution of TEOA (10 vol%) by a magnetic stirrer in Pyrex reaction vessel. The above suspension was evacuated 30 min to remove air prior to irradiation under a 300 W xenon lamp (PLS-SXE300UV, Perfectlight). $\lambda \geq 420$ nm cut-off filter was used for visible light irradiation (light intensity was determined to be 1.75 W/cm^2 by an PL-MW2000 photoradiometer, Perfectlight), 365 nm band-pass filter was used for UV light irradiation (light intensity is 74.4 mW/cm^2), and artificial solar light irradiation (light intensity is 2.14 W/cm^2) was provided without using any filters. The evolved hydrogen gas was circulated with a gas pump and quantified at a regular interval (1 h) by gas chromatography (Shiweipx GC7806) with thermal conductivity detector (TCD). The reactions were accomplished at 20 °C. The apparent quantum efficiency (AQE) value was calculated according to the following equation [8]. $AQE = \frac{2 \times \text{number of evolved H}_2 \text{ molecules}}{\text{number of incident photons}} \times 100\%$

3. Results and discussion

Ni species modified g-C$_3$N$_4$ synthesized by a simple impregnation method was annealed at different temperature for 3 h to change the phase and crystallinity of Ni species (Fig. 1). All samples were firstly evaluated by the X-ray diffraction (XRD). As shown in Fig. 2A, the XRD pattern of Ni/g-C$_3$N$_4$-100 shows the distinct diffraction peaks located at 32.9°, 38.5°, and 58.8° for the (100), (101), and (110) plane diffraction of β-Ni(OH)$_2$ nanocrystal (JCPDS No.14-0117) [19,30–34] and two distinct diffraction peaks (100) and (002) at 13.1° and 27.5° corresponding to the in-planar packing and the stacking of the conjugated aromatic system of host g-C$_3$N$_4$ [1,5,6,35]. With increasing the annealing temperature, the intensity of diffraction peaks for β-Ni(OH)$_2$ nanocrystal decreases and finally disappears (when the annealing temperature is higher than 300 °C) due to the thermal decomposition of Ni(OH)$_2$ according to the equation of Ni(OH)$_2$ = NiO + H$_2$O, which can be confirmed by the TEM and XPS results. However, for the Ni/g-C$_3$N$_4$-300 annealing at 300 °C, the signature diffraction peaks related to NiO species did not show up even if NiO amount increased up to 10.0% (Fig. 2B), indicated that the NiO species on Ni/g-C$_3$N$_4$-300 sample has the very low crystallinity and amorphous structure, which is verified by the TEM observations. After further increase of annealing temperature, the signature peaks of cubic phase NiO appear at 37.2°, 43.1°, 62.7°, 75.3°, and 79.3° corresponding to the (111), (200), (220), (311), and (222) plane diffraction (JCPDS No.47-1049) [34,36,37] and the peak intensity increases along with increased annealing temperature,

Fig. 2. (A) XRD patterns of g-C$_3$N$_4$ and Ni/g-C$_3$N$_4$-T obtained at different temperature. (B) XRD patterns of Ni$_x$/g-C$_3$N$_4$-300 with different Ni content.

suggesting the existence of crystalline NiO on both Ni/g-C$_3$N$_4$-400 and Ni/g-C$_3$N$_4$-500 (the crystallinity of NiO increases with the increase of annealing temperature). For comparison, two kind of NiO nanocrystal modified g-C$_3$N$_4$ samples with the same NiO content were prepared by the impregnation method (the sample denoted as Ni/g-C$_3$N$_4$-CI) and the hydrothermal method (the sample denoted as Ni/g-C$_3$N$_4$-CH). The diffraction peaks belong to cubic phase NiO clearly appear in the XRD patterns of Ni/g-C$_3$N$_4$-CI and Ni/g-C$_3$N$_4$-CH (Fig. S1), suggesting that nickel co-catalyst on Ni/g-C$_3$N$_4$-CI and Ni/g-C$_3$N$_4$-CH are mainly

Fig. 3. TEM and HRTEM images of (A) Ni/g-C$_3$N$_4$-100, (B) Ni/g-C$_3$N$_4$-200, (C and D) Ni/g-C$_3$N$_4$-300, (E) Ni/g-C$_3$N$_4$-400, and (F) Ni/g-C$_3$N$_4$-500.

crystalline NiO, which can be strongly confirmed by the TEM results (Fig. S2).

N$_2$ adsorption-desorption at 77 K was used to study the microstructural changes of the g-C$_3$N$_4$ before and after the modification of nickel species. The N$_2$ adsorption-desorption isotherm and the corresponding BJH pore-size distribution curves of g-C$_3$N$_4$ and Ni/g-C$_3$N$_4$-T are shown in Fig. S3. The isotherm patterns (Fig. S3A) with a clear H2 hysteresis loop at high relative pressures (p/p$_0$ > 0.5) for all photocatalysts can be identified as type IV according to the IUPAC classification, indicating the existence of mesopores in the sample. It is noted that nickel species loading leads to the reduced mesopores (as shown in Fig. S3B) and decreased BET surface area (the obtained specific BET surface area for g-C$_3$N$_4$, Ni/g-C$_3$N$_4$-100, Ni/g-C$_3$N$_4$-200, and Ni/g-C$_3$N$_4$-300 are 41.9, 31.3, 32.6 and 26.2 cm^2/g, respectively, Table S1) because of the most of nickel species loaded on the external surface of g-C$_3$N$_4$ block the mesoporous channels. When the treatment temperature is further increased (above 400 °C), thermal oxidation at high temperature could etches and tailors bulk structure of g-C$_3$N$_4$ [5,38] (also can be confirmed by the TEM results, see Fig. 3), which leads to the increased pore volume and BET surface area of Ni/g-C$_3$N$_4$-400 and Ni/g-C$_3$N$_4$-500 (surface area is 36.4 and 190.2 cm^2/g, respectively).

The structure and morphology of Ni-based species can be observed under transmission electron microscopy (TEM). As shown in TEM images of Ni/g-C$_3$N$_4$-100 and Ni/g-C$_3$N$_4$-200 (Fig. 3A and B), the belt-
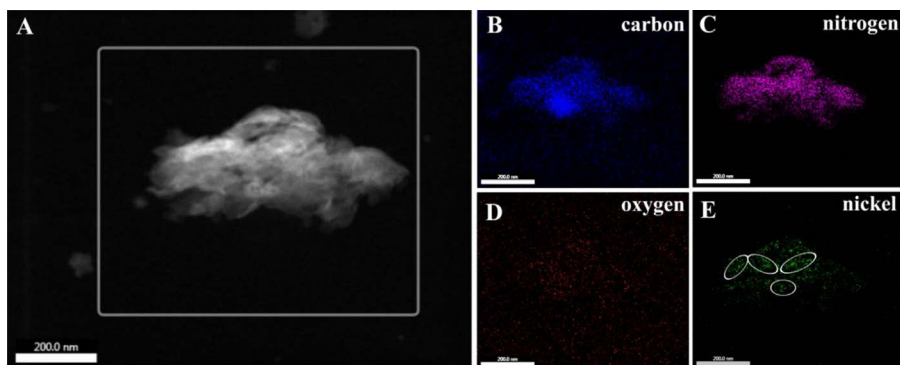
Fig. 4. STEM image and element mapping of C, N, O, and Ni in Ni/g-C$_3$N$_4$-300.

like nickel co-catalysts with length of about 80–100 nm are deposited on the surface of g-C$_3$N$_4$ nanosheets. The HRTEM images (inset of Fig. 3A and B) display a typical lattice fringe with d-spacing of ~ 0.27 nm, corresponding to the (010) plane of β-Ni(OH)$_2$ [33]. For the Ni/g-C$_3$N$_4$-300, the nickel co-catalysts on the surface of g-C$_3$N$_4$ nanosheets also appear as belt-like structure, as shown in Fig. 3C. These Ni species are believed as nickel oxide species according to the thermal decomposition of β-Ni(OH)$_2$, but the corresponding lattice fringes were not observed in HRTEM image (Fig. 3D) due to the amorphous structure of nickel species on Ni/g-C$_3$N$_4$-300. Nevertheless, EDX pattern (insert of Fig. 3C) illustrates the obvious fluorescent signals corresponding to O and Ni in the marked rectangular area of TEM image (Fig. 3C and D). Moreover, it can be also seen from the HRTEM image (Fig. 3D) that Ni species co-catalyst intimately contact with the g-C$_3$N$_4$ based on their different contrast, suggesting the formation of the amorphous NiO/g-C$_3$N$_4$ junction at the interface between amorphous NiO (the chemical states of Ni species can be verified by the XPS analyses) and g-C$_3$N$_4$. The surface structure and distribution of nickel oxide species on the Ni/g-C$_3$N$_4$-300 sample are further verified by performing dark-field TEM analysis with elemental mapping analysis (Fig. 4). The elemental mapping on the rectangular area shown in Fig. 4 B–E demonstrates a distribution of C, N, O and Ni atoms on the surface of the Ni/g-C$_3$N$_4$-300 sample, which further confirms the existence of nickel oxide species and the formation of phase junction. These observations suggest that the nickel oxide species on Ni/g-C$_3$N$_4$-300 sample has amorphous structure. After annealing sample at higher temperature (400 °C), the nickel co-catalysts will reconstruct and crystallize upon thermal treatment and oxidation. As shown in Fig. 3E, TEM image of Ni/g-C$_3$N$_4$-400 shows that the NiO co-catalysts with the size of about 5 nm are dispersed on g-C$_3$N$_4$ nanosheet. When the annealing temperature is up to 500 °C, the g-C$_3$N$_4$ substrate can be etched and exfoliated by thermally oxidized to form the porous nanosheets, and NiO nanoparticles with the size of 5 nm is highly dispersed on its surface, as shown in TEM image of Ni/g-C$_3$N$_4$-500 in Fig. 3F. HRTEM images of both Ni/g-C$_3$N$_4$-400 and Ni/g-C$_3$N$_4$-500 (inserts of Fig. 3E and F) show a typical lattice fringe with d spacing of ~ 0.21 nm, which is indexed as the (200) plane of cubic phase NiO [37,39].

Then, XPS analysis was carried out to identify the chemical composition of nickel species on the prepared samples and to elucidate the interaction between Ni species co-catalysts and g-C$_3$N$_4$ support. The Ni 2p, C 1s, N 1s, and O 1s XPS spectra and peak assignments of all samples are shown in Fig. 5, Fig. 6 and S8 and Table S2. Fig. 5 compares the high-resolution Ni 2p XPS spectra of Ni/g-C$_3$N$_4$-T (T = 100, 200, 300, 400, and 500) obtained at different annealing temperature. For Ni/g-C$_3$N$_4$-100 (Fig. 5B), the Ni 2p$_{3/2}$ signal can be fitted into a strong peak centered at around 855.9 eV and a weak peak at 855.1 eV. According to the results shown in Fig. 5A and literatures [19,34,39–43], these two peaks can be attributed to the Ni^{2+} cations in Ni(OH)$_2$ and NiO, respectively. It is note that the annealing treatment leads to changes of the surface Ni(OH)$_2$/NiO ratio, which decreases with the increase of annealing temperature (the Ni 2p$_{3/2}$ curves of Ni/g-C$_3$N$_4$-

300, Ni/g-C$_3$N$_4$-400, and Ni/g-C$_3$N$_4$-500 samples just show a strong peak centered at around 855.6 eV for Ni^{2+} cations in NiO, as shown in Fig. 5D–F). Correspondingly, O 1s peak at 530.0 eV for lattice oxygen of NiO increases with the increase of annealing temperature (Fig. S8 in supporting information) [34,43,44]. These results suggest that the Ni (OH)$_2$ on g-C$_3$N$_4$ surfaces are gradually converted into NiO through pyrolysis during the annealing process, which are well consistent with XRD and TEM results.

Fig. 6 shows the high-resolution C 1s and N 1s XPS spectra of g-C$_3$N$_4$, Ni/g-C$_3$N$_4$-100, Ni/g-C$_3$N$_4$-200, Ni/g-C$_3$N$_4$-300, Ni/g-C$_3$N$_4$-400, and Ni/g-C$_3$N$_4$-500. As shown in Fig. 6A, the C 1s peak of the sp^2 C=N bond in the *s*-triazine ring for Ni/g-C$_3$N$_4$-T shifts to the lower binding energy as compared to that for bare g-C$_3$N$_4$ [4,35] and the binding energy shift gradually increases with the increase of annealing temperature, suggesting that nickel species modification causes the increase in the electron density of g-C$_3$N$_4$. However, the binding energy shift of N 1s signals (at 398.4 eV, 499.8 eV, and 400.9 eV for sp^2-hybridized nitrogen in triazine rings, tertiary nitrogen N-(C)$_3$ groups, amino functions caring hydrogen) [4,35] for Ni/g-C$_3$N$_4$-T is not obvious (Fig. 6B). Correspondingly, the binding energy of Ni 2p$_{2/3}$ and O 1s for NiO on Ni/g-C$_3$N$_4$-300, Ni/g-C$_3$N$_4$-400, Ni/g-C$_3$N$_4$-500 samples increase as compared to NiO reference (Fig. 5, S8 and Table S2). These findings suggest the formation of NiO/g-C$_3$N$_4$ heterojunctions at the interface between NiO and g-C$_3$N$_4$.

The effect of nickel species modification on the optical properties of g-C$_3$N$_4$ was studied via UV–vis DRS and photoluminescence (PL) spectroscopy. Fig. 7A shows the UV–vis DRS spectra of g-C$_3$N$_4$, Ni/g-C$_3$N$_4$-100, Ni/g-C$_3$N$_4$-200, Ni/g-C$_3$N$_4$-300, Ni/g-C$_3$N$_4$-400, and Ni/g-C$_3$N$_4$-500. The spectra of both Ni/g-C$_3$N$_4$-100 and Ni/g-C$_3$N$_4$-200 show a broad absorption in the visible light region (600–800 nm) caused by the Ni(OH)$_2$ (because the absorption spectrum of the Ni(OH)$_2$ sample presents two wide absorptions centered at 390–450 nm and 600–800 nm [19,45]), and a slight red-shift of absorption edge (Fig. 7A and B) due to the existence of small amount of amorphous NiO (as evidenced by XPS). For amorphous NiO modified g-C$_3$N$_4$ sample (Ni/g-C$_3$N$_4$-300), the absorption edged red shifts to 460 nm and the absorption in the visible light region (400–800 nm) significantly increases (Fig. 7A and B). With increasing preparation temperature from 300 to 500 °C, the light absorption thresholds of obtained samples gradually shift from 460 to 755 nm (Fig. 7A). Correspondingly, the estimated band-gaps decrease from 2.60 eV to 2.20 eV (Fig. 7B). This result indicates that the NiO loading strongly influences electronic structure and optical absorption properties of g-C$_3$N$_4$.

The photoluminescence (PL) spectra of the samples were tested at room temperature with an excitation wavelength of 380 nm. As shown in Fig. 7C, the Ni/g-C$_3$N$_4$-100 shows decreased PL intensity as compared to that of bare g-C$_3$N$_4$, suggesting that the radiative charge recombination is inhibited by the Ni(OH)$_2$ loading. With the increasing of temperature (< 300 °C), Ni(OH)$_2$ species gradually decomposed into amorphous NiO, which leads to the decreased PL intensity. Moreover, PL intensity of Ni$_x$/g-C$_3$N$_4$-300 gradually decreases with the increase of
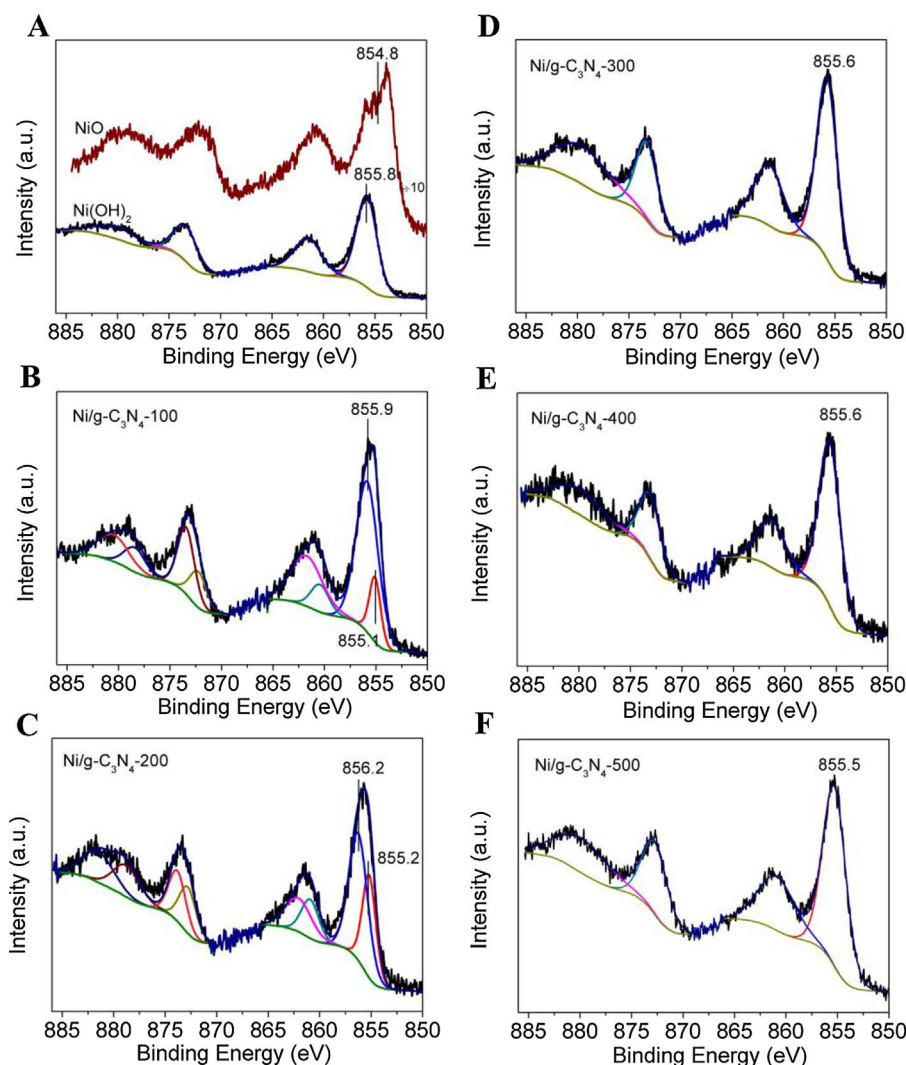
Fig. 5. High-resolution Ni 2p XPS spectra of (A) NiO and Ni$(OH)_2$, (B) Ni/g-C_3N_4-100, (C) Ni/g-C_3N_4-200, (D) Ni/g-C_3N_4-300, (E) Ni/g-C_3N_4-400, and (F) Ni/g-C_3N_4-500.

NiO content, as shown in Fig. 7D. These results indicate that the NiO co-catalysts on g-C_3N_4 are able to effectively promote the transfer of charge and thus inhibit the radiative charge recombination. Further increasing temperature leads to the decreased PL intensity, which might be due to the more intimate contact between crystalline NiO and host g-C_3N_4 and etched structure of g-C_3N_4. To eliminate the influence of texture, we compared the PL spectra of Ni/g-C_3N_4-300, Ni/g-C_3N_4-CI, and Ni/g-C_3N_4-CH samples to further investigate the effect of amorphous NiO on radiative charge recombination (Fig. S11). It is found that the PL intensity of Ni/g-C_3N_4-300 is the lowest among all the samples, in agreement with photocatalytic activity results.

Photocatalytic H_2 production activity for various samples was evaluated using triethanolamine as an electron donor. Fig. 8A and S12 show hydrogen generation over Ni_x/g-C_3N_4-300 with different NiO amount under visible light ($\lambda > 420$ nm) irradiation for 6 h. It can be clearly seen that the optimized amount of nickel species loading is 9.0 wt.% in terms of the activity for H_2 evolution. To understand effects of phase composition and crystallinity of Ni species on the photocatalytic activity for H_2 evolution, we evaluated the photocatalytic H_2 production activity of Ni/g-C_3N_4-T obtained at different annealing temperature (Fig. 8B and S13A) under visible light irradiation. It is found that β-Ni$(OH)_2$ co-catalyst modified g-C_3N_4 sample (Ni/g-C_3N_4-100, 15.0 μmol h^{-1} g^{-1}) shows enhanced photocatalytic H_2 evolution as compared to the unmodified g-C_3N_4 photocatalyst (0.16 μmol h^{-1} g^{-1}), suggesting that the Ni$(OH)_2$ co-catalysts be able to accelerate the transfer of photogenerated electrons, consequently

promote charge separation and H_2 evolution [19]. After annealing at low temperature (< 300 °C), H_2 evolution rates of samples in which the nickel species convert from Ni$(OH)_2$ nanocrystal to amorphous NiO increase dramatically with the increase of annealing temperature, and the maximum H_2 evolution rate of 68.8 μmol h^{-1} g^{-1} (nearly 430 times higher than that of unmodified g-C_3N_4) is achieved on the Ni/g-C_3N_4-300 sample (the NiO co-catalysts on Ni/g-C_3N_4-300 has amorphous structure). However, when the annealing temperature increased to above 400 °C, the photocatalytic activities of the samples gradually decrease (1.3 μmol h^{-1} g^{-1} and 0.96 μmol h^{-1} g^{-1} for Ni/g-C_3N_4-400 and Ni/g-C_3N_4-500). Similar comparison results are also observed for photocatalytic H_2 evolution under UV light or solar light irradiation (Fig. S13). This is due to the enhanced crystallinity of NiO on g-C_3N_4, as evidenced by the XRD, TEM and XPS results (Figs. 2–6).

To further confirm the great roles of crystallinity of NiO co-catalyst in photocatalytic water splitting, we have also carried out comparison tests by using two NiO nanocrystal modified g-C_3N_4 samples, prepared by the impregnation method (Ni/g-C_3N_4-CI) and the hydrothermal method (Ni/g-C_3N_4-CH), as control samples. The XRD, TEM, XPS, UV–vis absorption characterizations (Fig. S1, S2, S9, and S10 in supporting information) indicate that Ni species on both control samples present crystalline NiO. As shown in Fig. 8C and S14, the photocatalytic H_2 evolution rates over both control samples are obviously lower than that of amorphous NiO loaded sample Ni/g-C_3N_4-300. Also, the Ni/g-C_3N_4-CI with lower crystallinity of NiO exhibits higher H_2 evolution rate, whereas the Ni/g-C_3N_4-CH with higher crystallinity of NiO shows
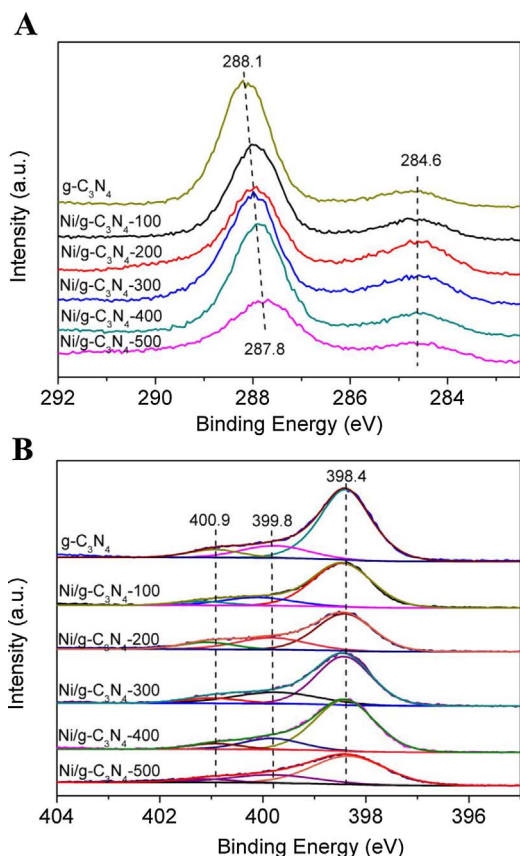
A

B

Fig. 6. High-resolution C 1 s (A) and N 1 s (B) XPS spectra of g-C$_3$N$_4$, Ni/g-C$_3$N$_4$-100, Ni/g-C$_3$N$_4$-200, Ni/g-C$_3$N$_4$-300, Ni/g-C$_3$N$_4$-400, and Ni/g-C$_3$N$_4$-500.

lower H$_2$ evolution rate. Therefore, based on these observations, we can conclude that the amorphous NiO species is more conducive to the hydrogen evolution over g-C$_3$N$_4$.

The photocurrent test of samples was employed to further investigate the electron transport and photoactivity. Fig. 9A shows photocurrent density curves of g-C$_3$N$_4$, Ni/g-C$_3$N$_4$-300, Ni/g-C$_3$N$_4$-400, and Ni/g-C$_3$N$_4$-500 photoanode chopping in 0.5 M Na$_2$SO$_4$ electrolyte under visible light irradiation. It appears that the amorphous NiO modification causes a remarkable improvement in photocurrent, and the photocurrent intensity decreases in the order of Ni/g-C$_3$N$_4$-300 > Ni/g-C$_3$N$_4$-400 > Ni/g-C$_3$N$_4$-500 with increasing of annealing temperature (in parallel with the photocatalytic activity results reported above). In addition, the electrochemical impedance spectrum (Fig. S15) shows that the Ni/g-C$_3$N$_4$-300 has the lowest resistance in electron transport. These results indicate that the amorphous structure of NiO greatly promotes the separation of photogenerated electron-hole pairs of g-C$_3$N$_4$ compared to crystalline NiO. To further verify the deduction, we performed the photoelectrochemical characterizations for Ni/g-C$_3$N$_4$-300, Ni/g-C$_3$N$_4$-CI, and Ni/g-C$_3$N$_4$-CH, as shown in Fig. 9B. As expected, the variation trend of photocurrent intensity for these samples under visible light irradiation is also in parallel with that of photocatalytic activity and PL results (Fig. S11).

To elucidate the roles of amorphous NiO co-catalysts in photocatalytic H$_2$ evolution, we deposited Pt co-catalysts on g-C$_3$N$_4$ and Ni/g-C$_3$N$_4$-300 samples (Pt/g-C$_3$N$_4$ and Pt/Ni/g-C$_3$N$_4$-300) using the *in-situ* photodeposition method and examined their photocatalytic hydrogen evolution activity, as shown in Fig. 10. It is interesting to note that the hydrogen evolution rate of Pt co-catalysts modified Ni/g-C$_3$N$_4$-300 significantly decreases as compared to Pt/g-C$_3$N$_4$, which shows the parallel and competitive effect of NiO species and Pt (the Fermi energies of Pt and NiO are more positive than g-C$_3$N$_4$, which causes electrons to move from g-C$_3$N$_4$ to the co-catalyst) [46]. This result indicates that the amorphous NiO serve as an electron acceptor and an active site for H$_2$ evolution.

Finally, to figure out more details on the enhanced visible-light activity, we have investigated the apparent quantum efficiency (AQE) at different irradiation wavelength, as shown in Fig. 8D. As compared to bare g-C$_3$N$_4$ (the g-C$_3$N$_4$ only shows activity at irradiation wavelength below 450 nm), the action spectrum threshold for Ni/g-C$_3$N$_4$-300 is up to 500 nm (AQE = 0.01%). The photons at wavelengths over 500 nm absorbed by Ni/g-C$_3$N$_4$-300 (Fig. 7) cannot result in H$_2$ generation, which implies that the excitation at > 500 nm light could not generates electrons with sufficient energy for H$^+$ reduction.

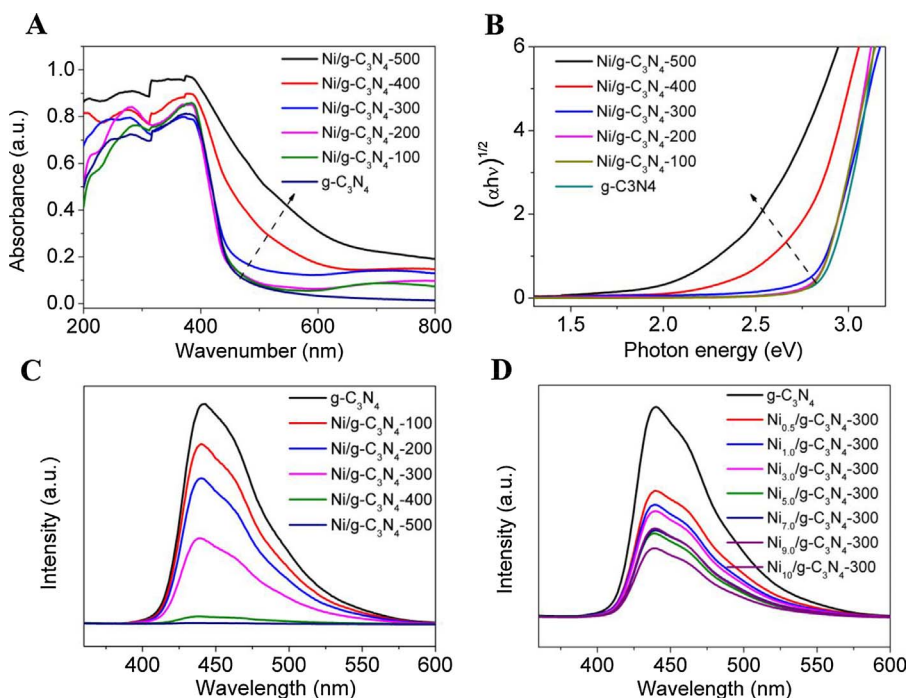The stability of Ni/g-C$_3$N$_4$-300 in the visible-light photocatalytic H$_2$

A

B

C

D

Fig. 7. (A) UV–vis DRS spectra of g-C$_3$N$_4$, Ni/g-C$_3$N$_4$-100, Ni/g-C$_3$N$_4$-200, Ni/g-C$_3$N$_4$-300, Ni/g-C$_3$N$_4$-400, and Ni/g-C$_3$N$_4$-500. (B) Tauc plot of g-C$_3$N$_4$, Ni/g-C$_3$N$_4$-100, Ni/g-C$_3$N$_4$-200, Ni/g-C$_3$N$_4$-300, Ni/g-C$_3$N$_4$-400, and Ni/g-C$_3$N$_4$-500. (C) PL spectra of g-C$_3$N$_4$, Ni/g-C$_3$N$_4$-100, Ni/g-C$_3$N$_4$-200, Ni/g-C$_3$N$_4$-300, Ni/g-C$_3$N$_4$-400, and Ni/g-C$_3$N$_4$-500. (D) PL spectra of Ni$_x$/g-C$_3$N$_4$-300 with different NiO content.
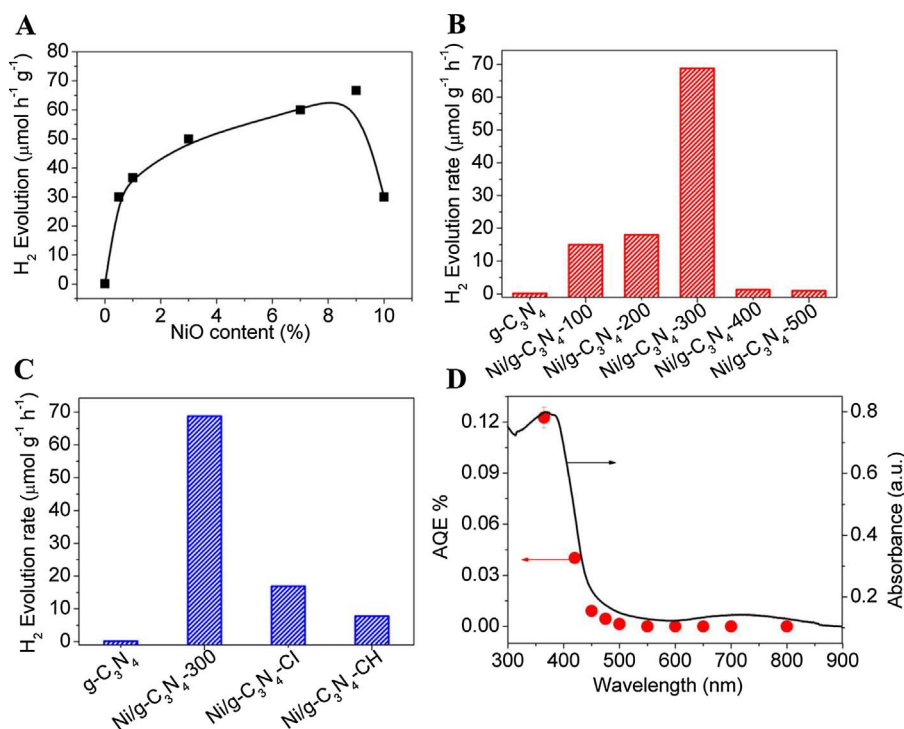
Fig. 8. (A) Hydrogen generation rate of $Ni_x/g-C_3N_4$-300 with different NiO amount under visible light ($\lambda > 420$ nm) irradiation (6 h). (B) photocatalytic H_2 evolution over $g-C_3N_4$, $Ni/g-C_3N_4$-100, $Ni/g-C_3N_4$-200, $Ni/g-C_3N_4$-300, $Ni/g-C_3N_4$-400, and $Ni/g-C_3N_4$-500 under visible light ($\lambda > 420$ nm) irradiation (6 h). (C) $g-C_3N_4$, $Ni/g-C_3N_4$-300, $Ni/g-C_3N_4$-CI, and $Ni/g-C_3N_4$-CH under visible light ($\lambda > 420$ nm) irradiation (6 h). (D) wavelength-dependent quantum efficiency (photon-to-H_2 evolution) over the $Ni/g-C_3N_4$-300 sample.
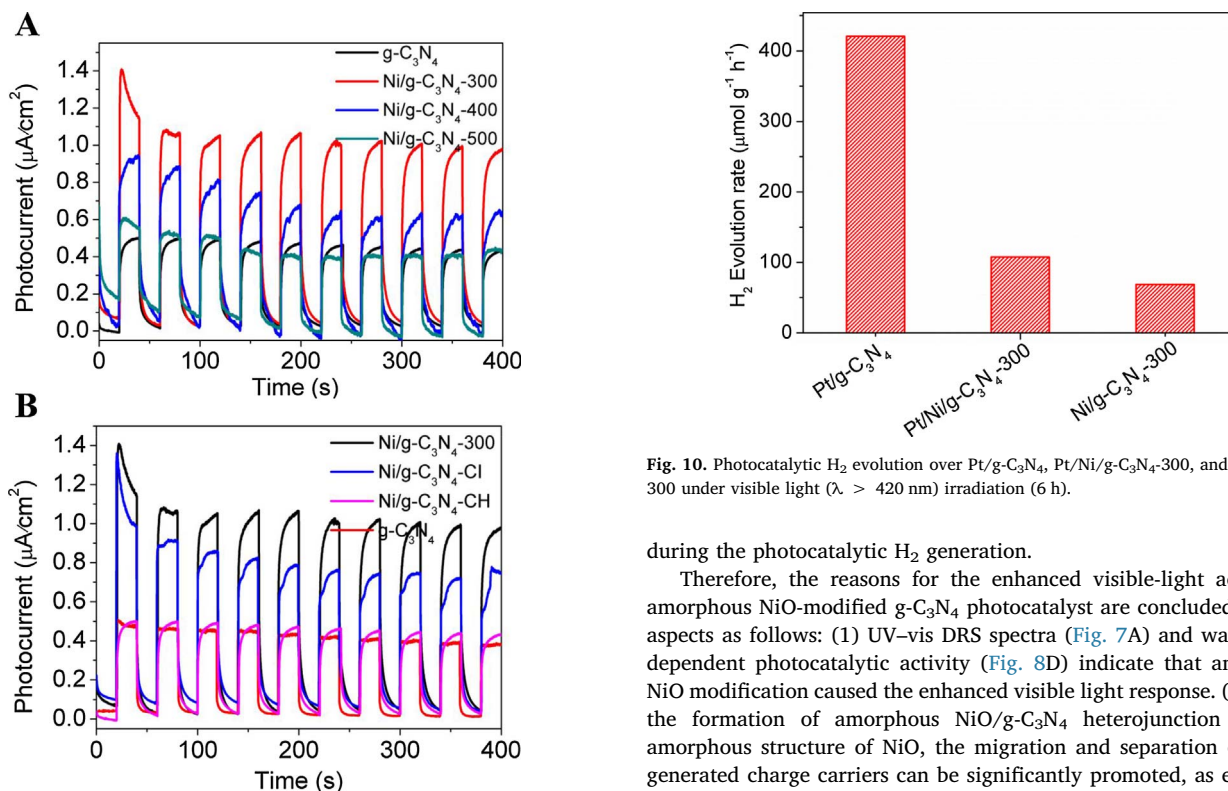

Fig. 9. (A) Photocurrent (i-t curve) of $g-C_3N_4$, $Ni/g-C_3N_4$-300, $Ni/g-C_3N_4$-400, and $Ni/g-C_3N_4$-500. (B) photocurrent (i-t curve) of $g-C_3N_4$, $Ni/g-C_3N_4$-300, $Ni/g-C_3N_4$-CI, and $Ni/g-C_3N_4$-CH.

Fig. 10. Photocatalytic H_2 evolution over $Pt/g-C_3N_4$, $Pt/Ni/g-C_3N_4$-300, and $Ni/g-C_3N_4$-300 under visible light ($\lambda > 420$ nm) irradiation (6 h).

during the photocatalytic H_2 generation.

Therefore, the reasons for the enhanced visible-light activity of amorphous NiO-modified $g-C_3N_4$ photocatalyst are concluded as three aspects as follows: (1) UV–vis DRS spectra (Fig. 7A) and wavelength-dependent photocatalytic activity (Fig. 8D) indicate that amorphous NiO modification caused the enhanced visible light response. (2) Due to the formation of amorphous $NiO/g-C_3N_4$ heterojunction and the amorphous structure of NiO, the migration and separation of photo-generated charge carriers can be significantly promoted, as evidenced by results of PL (Fig. 7 and S11) and photocurrent (Fig. 9). (3) Like the NiO_x clusters or single sites, the amorphous NiO co-catalysts provide more active sites for H_2 evolution (Figs. 8–10).

According to the above mentioned results and band structure of NiO and $g-C_3N_4$, the mechanism for the photocatalytic H_2 evolution over $Ni/g-C_3N_4$-300 is proposed and illustrated in Scheme 1. Under visible light irradiation (420 nm $< \lambda <$ 450 nm), amorphous $NiO/g-C_3N_4$ heterojunctions create an inner electric field at the interface, which allows for the transfer of the photogenerated electrons of $g-C_3N_4$ (conduction band potentials $E_{CB} = -1.12$ V vs NHE [47]) across the

generation was evaluated by re-cycling the reaction under the same conditions. As shown in Fig. S16, the photocatalytic H_2 evolution rate over $Ni/g-C_3N_4$-300 is well maintained after five test cycles. Moreover, the structure of $Ni/g-C_3N_4$-300 and chemical state of Ni species on $Ni/g-C_3N_4$-300 remained no change after reaction (Fig. S17 and S18). These results indicate that the $Ni/g-C_3N_4$-300 photocatalyst is well stable
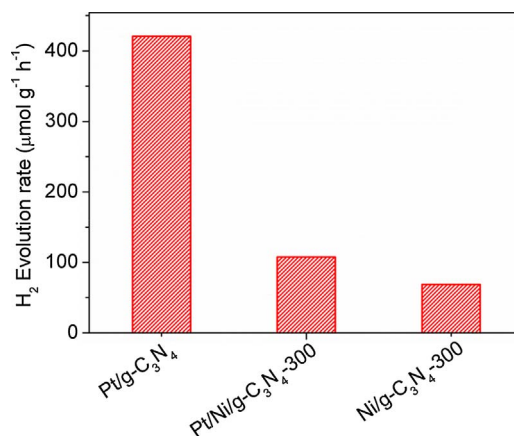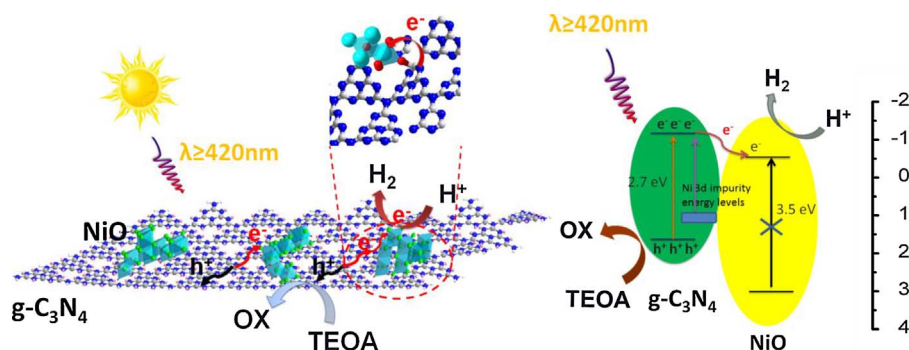
interfacial C−O−Ni linkages to amorphous NiO co-catalysts (conduction band potentials $E_{CB} = -0.5$ V vs NHE [48–50]) for proton reduction into H_2. The sacrificial electron donor TEOA can be oxidized by the photogenerated holes on surface of g-C_3N_4. Moreover, amorphous of NiO loading provides the impurity energy level, which caused the broadened visible light absorption and response of Ni/g-C_3N_4-300 (as shown in Fig. 7A and Fig. 8D). Therefore, under > 450 nm visible light irradiation, the electrons can be excited from Ni 3d state of the Ni^{2+} doping [51] caused by loading of amorphous NiO co-catalyst to the conduction band of g-C_3N_4 for proton reduction into H_2.

4. Conclusions

An amorphous NiO modified g-C_3N_4 non-noble metal photocatalyst is prepared through the wetness impregnation method with post thermal treatment at 300 °C. The amorphous NiO co-catalysts provide more active sites for H_2 evolution and amorphous NiO modification causes the enhanced visible light response. Moreover, amorphous NiO/g-C_3N_4 heterojunctions formed at interface between amorphous NiO and host g-C_3N_4 create an inner electric field at the interface, which allow for the transfer of the photogenerated electrons of g-C_3N_4 across the interfacial C−O−Ni linkages to amorphous NiO co-catalysts and thus significantly promote the migration and separation of photogenerated charge carriers. Therefore, amorphous NiO modified g-C_3N_4 non-noble metal photocatalysts shows significantly enhanced visible-light photocatalytic hydrogen production activity as compared to bare g-C_3N_4 and crystalline NiO modified g-C_3N_4 photocatalysts.

Acknowledgements

Appendix A. Supplementary data

Supplementary data associated with this article can be found, in the online version, at http://dx.doi.org/10.1016/j.apcatb.2017.09.073.

References

[1] X. Wang, K. Maeda, A. Thomas, K. Takanabe, G. Xin, J.M. Carlsson, K. Domen, M. Antonietti, Nat. Mater. 8 (2009) 76–80.
[2] S. Cao, J. Low, J. Yu, M. Jaroniec, Adv. Mater 27 (2015) 2150–2176.
[3] W. Che, W. Cheng, T. Yao, F. Tang, W. Liu, H. Su, Y. Huang, Q. Liu, J. Liu, F. Hu, Z. Pan, Z. Sun, S. Wei, J. Am. Chem. Soc. 139 (2017) 3021–3026.
[4] Q. Gu, Z. Gao, C. Xue, Small 12 (2016) 3543–3549.
[5] Q. Gu, Z. Gao, H. Zhao, Z. Lou, Y. Liao, C. Xue, RSC Adv. 5 (2015) 49317–49325.
[6] Q. Gu, Y. Liao, L. Yin, J. Long, X. Wang, C. Xue, Appl. Catal. B: Environ. 165 (2015) 503–510.
[7] Q. Gu, J. Liu, Z. Gao, C. Xue, Chem.–Asian J. 11 (2016) 3169–3173.
[8] J. Liu, Y. Liu, N. Liu, Y. Han, X. Zhang, H. Huang, Y. Lifshitz, S.-T. Lee, J. Zhong, Z. Kang, Science 347 (2015) 970–974.
[9] W.-J. Ong, L.-L. Tan, Y.H. Ng, S.-T. Yong, S.-P. Chai, Chem. Rev. 116 (2016) 7159–7329.
[10] H. Ou, L. Lin, Y. Zheng, P. Yang, Y. Fang, X. Wang, Adv. Mater. 29 (2017) 1700008, http://dx.doi.org/10.1002/adma.201700008.
[11] Z. Zhang, J. Huang, J. Fang, M. Zhang, K. Liu, B. Dong, Adv. Mater 29 (2017) 1606688.
[12] C. Han, L. Wu, L. Ge, Y. Li, Z. Zhao, Carbon 92 (2015) 31–40.
[13] J. Xue, S. Ma, Y. Zhou, Z. Zhang, M. He, ACS Appl. Mater. Inter. 7 (2015) 9630–9637.
[14] C. Yang, B. Wang, L. Zhang, L. Yin, X. Wang, Angew. Chem. Int.Edit. 56 (2017) 6627–6631.
[15] G. Zhang, Z.-A. Lan, L. Lin, S. Lin, X. Wang, Chem. Sci. 7 (2016) 3062–3066.
[16] Y. Zhang, J. Liu, G. Wu, W. Chen, Nanoscale 4 (2012) 5300–5303.
[17] D.H. Wang, J.N. Pan, H.H. Li, J.J. Liu, Y.B. Wang, L.T. Kang, J.N. Yao, J. Mater. Chem. A 4 (2016) 290–296.
[18] Y. Zhu, Y. Xu, Y. Hou, Z. Ding, X. Wang, Int. J. Hydrogen Energ. 39 (2014) 11873–11879.
[19] J. Yu, S. Wang, B. Cheng, Z. Lin, F. Huang, Catal. Sci. Technol. 3 (2013) 1782–1789.
[20] J. Hong, Y. Wang, Y. Wang, W. Zhang, R. Xu, ChemSusChem 6 (2013) 2263–2268.
[21] L. Liu, Y. Qi, J. Hu, Y. Liang, W. Cui, Appl. Surf. Sci. 351 (2015) 1146–1154.
[22] W. Chen, T.-Y. Liu, T. Huang, X.-H. Liu, J.-W. Zhu, G.-R. Duan, X.-J. Yang, J. Mater. Sci. 50 (2015) 8142–8152.
[23] C. Kong, S. Min, G. Lu, Chem. Commun. 50 (2014) 5037–5039.
[24] J. Yuan, J. Wen, Q. Gao, S. Chen, J. Li, X. Li, Y. Fang, Dalton Trans. 44 (2015) 1680–1689.
[25] M. Liu, X. Qiu, M. Miyauchi, K. Hashimoto, Chem. Mater 23 (2011) 5282–5286.
[26] L. Chen, Q. Gu, L. Hou, C. Zhang, Y. Lu, X. Wang, J. Long, Catal. Sci. Technol. 7 (2017) 2039–2049.
[27] L. Fan, J. Long, Q. Gu, H. Huang, H. Lin, X. Wang, J. Catal. 320 (2014) 147–159.
[28] X. Li, W. Bi, L. Zhang, S. Tao, W. Chu, Q. Zhang, Y. Luo, C. Wu, Y. Xie, Adv. Mater. 28 (2016) 2427–2431.
[29] C. Han, Y. Lu, J. Zhang, L. Ge, Y. Li, C. Chen, Y. Xin, L. Wu, S. Fang, J. Mater. Chem. A 3 (2015) 23274–23282.
[30] W. Zhou, M. Yao, L. Guo, Y. Li, J. Li, S. Yang, J. Am. Chem. Soc. 131 (2009) 2959–2964.
[31] F.-S. Cai, G.-Y. Zhang, J. Chen, X.-L. Gou, H.-K. Liu, S.-X. Dou, Angew. Chem. Int. Edit. 43 (2004) 4212–4216.
[32] Z. Lu, Z. Chang, W. Zhu, X. Sun, Chem. Commun. 47 (2011) 9651–9653.
[33] X. Wang, Q. Zhu, H. Zhang, Chem. Commun. (2005) 5231–5233.
[34] S. Tong, M. Zheng, Y. Lu, Z. Lin, J. Li, X. Zhang, Y. Shi, P. He, H. Zhou, J. Mater. Chem. A 3 (2015) 16177–16182.
[35] A. Thomas, A. Fischer, F. Goettmann, M. Antonietti, J.-O. Muller, R. Schlogl, J.M. Carlsson, J. Mater. Chem. 18 (2008) 4893–4908.
[36] G.-J. Li, X.-X. Huang, Y. Shi, J.-K. Guo, Mater. Lett. 51 (2001) 325–330.
[37] C.-Y. Cao, W. Guo, Z.-M. Cui, W.-G. Song, W. Cai, J. Mater. Chem. 21 (2011) 3204–3209.
[38] P. Niu, L. Zhang, G. Liu, H.-M. Cheng, Adv. Funct. Mater. 22 (2012) 4763–4770.
[39] Y. Cheng, J. Pan, M. Saunders, S. Yao, P.K. Shen, H. Wang, S.P. Jiang, RSC Adv. 6 (2016) 51356–51366.
[40] J. Wang, S. Mao, Z. Liu, Z. Wei, H. Wang, Y. Chen, Y. Wang, ACS Appl. Mater. Inter. 9 (2017) 7139–7147.
[41] Y. Takahashi, T. Tatsuma, Langmuir 21 (2005) 12357–12361.
[42] S. Anantharaj, P.E. Karthik, S. Kundu, Catal. Sci. Technol. 7 (2017) 882–893.
[43] U. St, C. Scharfschwerdt, M. Neumann, G. Illing, H.J. Freund, J. Physics: Condens. Mat. 4 (1992) 7973.
[44] A.G. Marrani, V. Novelli, S. Sheehan, D.P. Dowling, D. Dini, ACS Appl. Mater. Inter. 6 (2014) 143–152.
[45] Y. Qi, H. Qi, J. Li, C. Lu, J. Cryst. Growth 310 (2008) 4221–4225.
[46] T.K. Townsend, N.D. Browning, F.E. Osterloh, Energy Environ. Sci. 5 (2012) 9543–9550.
[47] S.C. Yan, S.B. Lv, Z.S. Li, Z.G. Zou, Dalton Trans. 39 (2010) 1488–1491.
[48] Y. Xu, M.A.A. Schoonen, Am. Mineral. 85 (2000) 543–556.
[49] H. Kato, A. Kudo, J. Phys. Chem. B 105 (2001) 4285–4292.
[50] Y. Miseki, H. Kato, A. Kudo, Energy Environ. Sci. 2 (2009) 306–314.
[51] X. Wang, X. Chen, A. Thomas, X. Fu, M. Antonietti, Adv. Mater. 21 (2009) 1609–1612.